

## Article

# Ag-Mn<sub>x</sub>O<sub>y</sub> on Graphene Oxide Derivatives as Oxygen Reduction Reaction Catalyst in Alkaline Direct Ethanol Fuel Cells

Sigrid Wolf <sup>1,\*</sup>, Michaela Roschger <sup>1</sup>, Boštjan Genorio <sup>2</sup>, Mitja Kolar <sup>2</sup>, Daniel Garstenauer <sup>1</sup>, Brigitte Bitschnau <sup>3</sup> and Viktor Hacker <sup>1</sup>

- <sup>1</sup> Institute of Chemical Engineering and Environmental Technology, Graz University of Technology, Inffeldgasse 25/C, 8010 Graz, Austria; michaela.roschger@tugraz.at (M.R.); daniel.garstenauer@univie.ac.at (D.G.); viktor.hacker@tugraz.at (V.H.)
- <sup>2</sup> Faculty of Chemistry and Chemical Technology, University of Ljubljana, Večna pot 113, 1000 Ljubljana, Slovenia; bostjan.genorio@fkk.uni-lj.si (B.G.); mitja.kolar@fkk.uni-lj.si (M.K.)
- <sup>3</sup> Institute of Physical and Theoretical Chemistry, Graz University of Technology, Stremayrgasse 9, 8010 Graz, Austria; bitschnau@tugraz.at
- \* Correspondence: sigrid.wolf@tugraz.at

**Abstract:** In this study, Ag-Mn<sub>x</sub>O<sub>y</sub>/C composite catalysts deposited on reduced graphene oxide (rGO) and, for the first time on N-doped graphene oxide (NGO), were prepared via a facile synthesis method. The influence of the carbon support material on the activity and stability of the oxygen reduction reaction (ORR) and on the tolerance to ethanol in alkaline medium was focused and investigated. The physicochemical properties of the Ag-Mn<sub>x</sub>O<sub>y</sub>/C catalysts were analyzed by X-ray diffraction (XRD), scanning electron microscopy with energy dispersive X-ray spectroscopy (SEM-EDS), Brunauer–Emmett–Teller (BET) method, atomic absorption spectroscopy (AAS), inductively coupled plasma-mass spectrometry (ICP-MS), and thermogravimetric gas analysis (TGA). Electrochemical characterization was performed by rotating disk electrode (RDE) experiments. The results show that the active manganese species MnO<sub>2</sub> was assembled as nanorods and nanospheres on rGO and NGO, respectively. Ag was assumed to be present as very small or amorphous particles. Similar redox processes for Ag-Mn<sub>x</sub>O<sub>y</sub>/rGO and Ag-Mn<sub>x</sub>O<sub>y</sub>/NGO were examined via cyclic voltammetry. The Ag-Mn<sub>x</sub>O<sub>y</sub>/rGO resulted in a more negative diffusion limiting current density of  $-3.01 \text{ mA cm}^{-2}$  compared to Ag-Mn<sub>x</sub>O<sub>y</sub>/NGO. The onset potential of approximately 0.9 V vs. RHE and the favored 4-electron transfer pathway were independent of the support material. Ag-Mn<sub>x</sub>O<sub>y</sub>/NGO exhibited a higher ORR stability, whereas Ag-Mn<sub>x</sub>O<sub>y</sub>/rGO showed a better ethanol tolerance.

**Keywords:** ethanol tolerant oxygen reduction reaction catalysts; reduced graphene oxide; oxygen reduction reaction; alkaline direct ethanol fuel cell



**Citation:** Wolf, S.; Roschger, M.; Genorio, B.; Kolar, M.; Garstenauer, D.; Bitschnau, B.; Hacker, V. Ag-Mn<sub>x</sub>O<sub>y</sub> on Graphene Oxide Derivatives as Oxygen Reduction Reaction Catalyst in Alkaline Direct Ethanol Fuel Cells. *Catalysts* **2022**, *12*, 780. <https://doi.org/10.3390/catal12070780>

Academic Editor: Minhua Shao

Received: 16 June 2022

Accepted: 12 July 2022

Published: 14 July 2022

**Publisher's Note:** MDPI stays neutral with regard to jurisdictional claims in published maps and institutional affiliations.



**Copyright:** © 2022 by the authors. Licensee MDPI, Basel, Switzerland. This article is an open access article distributed under the terms and conditions of the Creative Commons Attribution (CC BY) license (<https://creativecommons.org/licenses/by/4.0/>).

## 1. Introduction

The global increase in greenhouse gas emissions due to the use of fossil fuels is forcing the increased use of alternative, cost-efficient, and renewable energy sources. Alkaline direct ethanol fuel cells (ADEFCS) have gained enormous attention in recent years, as the liquid energy carrier ethanol has a high energy density and is an environmentally friendly, easy to transport, non-toxic fuel that can be produced using agriculture products and biomass [1,2].

In addition to the problem of incomplete fuel oxidation at the anode, the commercialization of ADEFCS is hindered by the fact that expensive noble metals are still used in the cathode and the performance is reduced by the ethanol crossover from the anode to the cathode due to mixed potentials [3]. The development of low cost, highly efficient and tolerant catalysts for the oxygen reduction reaction at the cathode is therefore of major importance. Pt has usually been the state-of-the-art electrocatalyst for the oxygen reduction

reaction (ORR). Non-Pt catalyst alternatives have been extensively investigated in recent years [4,5], however, since Pt is restricted by major disadvantages, including very high costs, limited reserves in nature, durability issues, and its susceptibility to ethanol crossover. The research focuses partly on platinum-free metal catalysts, such as silver and its alloys, but mainly on doped carbons (especially graphene derivatives), transition metal oxides such as various perovskites, cobalt oxides, or manganese oxides, and on metal oxide/graphene composites [6–13].

Ag has been extensively identified as a promising cathode catalyst as it is cheaper than Pt, shows high ORR activity and stability in alkaline electrolytes, and is insensitive to alcohol crossover [14–16]. Truong et al. [17] found that the ORR activity on Ag/C is close to that on Pt. Alloying of Ag with other metals to produce silver nanoalloys electrocatalysts for ORR in alkaline media is also effective, as Qaseem et al. [6] stated in a detailed published review on recent advances. Despite the intensive research on Ag alloy catalysts, the performance is not yet sufficient, so the combination with transition metals is subject to increasing investigation.

Manganese oxides ( $Mn_xO_y$ ) have been identified as the most promising ORR catalysts in alkaline media as they bring advantages such as low cost and are associated with high abundant natural manganese ores, environmental friendliness, and high electrocatalytic activity towards ORR [10]. The ORR performance of  $Mn_xO_y$  catalysts depends on different parameters including preparation methods, manganese valence state, surface morphology, and crystalline structure [10,18,19]. The use and investigation of various  $MnO_2/C$  materials as efficient ORR catalysts in alkaline media was focused on intensively over many years. For example, Calegario et al. [20] already showed in 2005 that the relationship between  $Mn_xO_y$  and the carbon support plays an important role and can promote the preferential 4-electron pathway. The latest studies, however, also repeatedly prioritize the use of manganese oxides, as in a recent work by Purwaningsih et al. [13] in which they effectively prepared  $MnO_2$  nanorods on reduced graphene oxide by means of electrophoretic deposition.

Many studies have been reported in which Ag is combined with  $Mn_xO_y$  to benefit from the properties of both compounds [14,21–24]. The current density of Ag- $Mn_3O_4/C$  is almost 3.75 times higher compared to Ag/C, as described by Liu et al. [22]. A recent study by Marukawa et al. [25], in which Ag is deposited on  $MnO_2$ , also shows that the combination of Ag with  $MnO_2$  provides superior ORR activity compared to Ag. A higher stability and tolerance to alcohol fuel crossover compared to Pt/C can be achieved with Ag- $Mn_yO_x/C$  catalysts, as shown by Tang et al. [14].

Catalytic activity towards ORR is not only influenced by the active material itself, but the deposition of metals on a suitable carbon material and their individual characteristics also play a major role. Graphene derivatives, with their outstanding electronic, thermal, chemical, and mechanical properties [8], have proven to be an efficient catalyst support material [4,16,26]. Graphene presents a honeycomb-like structure consisting of  $sp^2$ -carbon atoms that reveals an ultra-high specific surface area, excellent electrical conductivity, together with thermal and chemical stability [4,7]. Graphene derivatives can appear in many different forms and their properties can vary greatly. The most frequently applied type as support material is reduced graphene oxide (rGO), which can be produced from graphene oxide (GO) via chemical or thermal reduction [27]. It is exfoliated in this form, and the structure of the rGO contains low quantities of oxygen-containing functional groups such as hydroxyls, epoxides, or carbonyls, as well as vacancy defects. These groups can promote the immobilization and anchoring and thus also the stability of the metal and metal oxide particles [7,27]. Lee et al. [4] already published that rGO can be used as efficient carbon support for silver manganese oxides.

In recent studies, more and more emphasis is being shifted to doping the graphene materials with heteroatoms [28]. The most studied method is doping with nitrogen, which results in N-doped graphene oxide (NGO), presenting several nitrogen chemical point defects in the 2D structure. Defects of this kind can be present as nitrogen functionalities, i.e., pyridinic-N, pyrrolic-N, and graphitic-N. There are several reports that show

that N-functionalities have an active role in electrocatalysis and could be beneficial for ORR [8,29–32]. Liu et al. [33] described that supporting  $\text{CoMn}_2\text{O}_4$  with nitrogen-doped graphene enhanced the electrochemical activity of the catalyst, which was attributed to the availability of more active sites, higher conductivity, and synergistic effects caused by the nitrogen atoms. The use of nitrogen-doped graphene oxide as a support material for Ag has also been investigated, and Linge et al. [34] demonstrated that high catalytic activity is achieved with Ag/NGO.

In this study, based on the above knowledge,  $\text{Ag-Mn}_x\text{O}_y$  was deposited as the active material on rGO and, for the first time, on NGO to investigate the influence of the support material on the activity and stability towards ORR as well as on the ethanol tolerance. The use of the new support materials, especially NGO, ensures a large specific surface area and a strong interaction with the active material, thus enhancing the activity and stability of the catalysts in terms of ORR. The catalysts were prepared by a simple adapted synthesis method and comprehensive physicochemical characterization was performed. The electrochemical properties were determined by rotating disk electrode (RDE) and the kinetic properties were evaluated by Koutecky–Levich analysis.

## 2. Results and Discussion

### 2.1. Physicochemical Characterization of ORR Catalysts

The activity of the catalysts towards ORR can be strongly affected by their physicochemical properties, dependent on their structure, morphology, and surface area, as well as on the nature of the carbon support material [16,32,35]. The following section presents comprehensive physicochemical characterization results for the synthesized  $\text{Ag-Mn}_x\text{O}_y/\text{rGO}$  and  $\text{Ag-Mn}_x\text{O}_y/\text{NGO}$  by means of XRD, SEM-EDS, BET, ICP-MS, AAS, and TGA-MS.

In this study, rGO and NGO were synthesized from the same GO precursor which was obtained from the graphite precursor oxidized and partially exfoliated using Hummers method. GO was chemically reduced using hydrazine hydrate as the reducing agent to obtain rGO with partially restored graphene honeycomb structure, which is responsible for electron conduction. On the other hand, NGO is also a material with a partially restored honeycomb structure with several nitrogen chemical point defects in the 2D structure. A defect of this kind can be present as nitrogen functionalities, i.e., pyridinic-N, pyrrolic-N, and graphitic-N. There are several reports that show that N-functionalities have an active role in electrocatalysis [29–32]. Such an effect could be beneficial for the ORR in direct alkaline ethanol fuel cells [8]. Further, the structure of the metals and metal oxides deposited on the carbon support material also plays a major role for the ORR activity. As for the manganese oxides, the catalytic activity is especially dependent on the Mn oxidation state as well as on the oxide structure [10,36]. The structure of the  $\text{Ag-Mn}_x\text{O}_y/\text{rGO}$  and  $\text{Ag-Mn}_x\text{O}_y/\text{NGO}$  catalysts and of the rGO and NGO support materials was analyzed using XRD. Figure 1 shows the XRD patterns of all materials and the diffraction peak positions, and relative intensities of the standard patterns of  $\text{MnO}_2$  (ICSD #29561),  $\text{Mn}_3\text{O}_4$  (ICSD #33327), Ag (ICSD #22434), and graphite (ICSD #18838) are included in the bottom for comparison.

The broad peak at  $2\theta$   $25.0^\circ$  and the one at  $43.0^\circ$  in the rGO-based patterns are attributable to graphite crystal facets (002) and (100), respectively [28,37]. The peak of the graphite plane (002) is sharper and shifted to  $26.5^\circ$  for the NGO materials, indicating that they present a higher crystallinity, the graphitic content is higher, and it is more reduced [30,38], which is also reflected by the presence of additional peaks at  $45.0^\circ$  and  $54.3^\circ$ , characteristic for the graphite structure [39]. These features may also hint that less exfoliation occurred compared to the rGO equivalents [8]. The patterns of  $\text{Ag-Mn}_x\text{O}_y/\text{C}$  catalysts are comparable to the  $\text{AgMnO}_x$ -fresh sample of Wu et al. [23]. The peaks at  $36.8^\circ$  and  $65.7^\circ$  can be attributed to the  $\text{MnO}_2$  (100) and (110), respectively. The flat broad peak between  $29.0^\circ$  and  $34.0^\circ$  indicates a minor portion of  $\text{Mn}_3\text{O}_4$  [23]. Many studies have found that the structure of the manganese oxides plays an important role in the activity of the ORR.  $\alpha\text{-MnO}_2$  is described to be the most active form [40]. In addition, the peaks are sharper for

Ag-Mn<sub>x</sub>O<sub>y</sub>/rGO, which indicates a higher crystallinity. The MnO<sub>2</sub> crystallite size of the two Ag-Mn<sub>x</sub>O<sub>y</sub>/C samples was estimated via Scherrer equation with the assumption of spherical particles and  $k = 0.9$ , as generally taken for powders. The average FWHM (full width at half maximum) of several peaks (36.8° and 65.7°) was used for calculation and a crystallite size of approximately 6.8 nm and 6.6 nm was determined for Ag-Mn<sub>x</sub>O<sub>y</sub>/NGO and Ag-Mn<sub>x</sub>O<sub>y</sub>/rGO, respectively. Ag peaks are not visible, as the material is probably amorphous or occurs in very small particle sizes [23]. No prediction can be made about the nature of the Ag species from this XRD data. It can only be confirmed using the data from the elemental analysis that Ag is present in the correct proportion. However, if it is considered that the diffractograms are very similar to the AgMnO<sub>x</sub>-fresh sample of Wu et al. [23], it is strongly assumed that Ag is present as Ag<sub>2</sub>O.

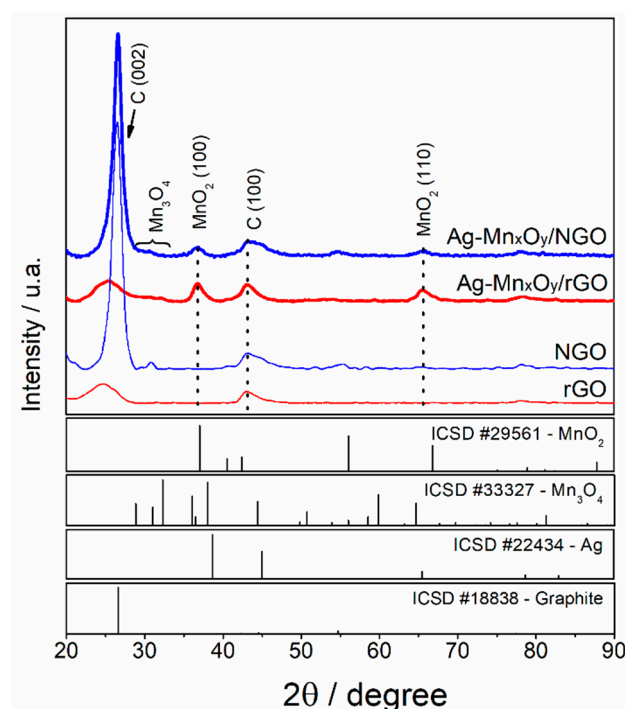


**Figure 1.** XRD patterns of rGO, NGO, Ag-Mn<sub>x</sub>O<sub>y</sub>/rGO, and Ag-Mn<sub>x</sub>O<sub>y</sub>/NGO with MnO<sub>2</sub>, Mn<sub>3</sub>O<sub>4</sub>, Ag, and graphite standard patterns from ICSD for comparison.

It has been shown previously that the morphology of graphene-based metal support and the metal itself have a great impact on the activity of the electrocatalyst [18,19,29,32]. To determine the morphology and specific surface area of the electrocatalysts, SEM and gas adsorption experiments were performed. Figure 2 shows the sheet-like structure which can be assigned to the graphene derivative support materials also found in the literature [29,31,38]. The morphological difference between rGO and NGO is clearly indicated. Chemical reduction with hydrazine furnished high surface area rGO support in the shape irregular spheres (lower magnification) but highly exfoliated crumpled structure (large magnification). However, NGO shows an irregular and flaky morphology (lower magnification) with exfoliated flat multilayer graphene sheets (higher magnification). The difference in morphology does not impact the specific area or porosity of Ag-Mn<sub>x</sub>O<sub>y</sub>/rGO and Ag-Mn<sub>x</sub>O<sub>y</sub>/NGO (Table 1, Figure S1). Both materials show a similar pore size and specific surface area of 244.6 m<sup>2</sup> g<sup>-1</sup> for Ag-Mn<sub>x</sub>O<sub>y</sub>/rGO and 285.7 m<sup>2</sup> g<sup>-1</sup> for Ag-Mn<sub>x</sub>O<sub>y</sub>/NGO. The main reason for the morphological difference is most probably the reduction protocol. rGO was the subject of a “wet chemistry” approach, i.e., chemical reduction in suspension, while NGO was a subject of a heat treatment protocol in NH<sub>3</sub> gas dry conditions. This means that the GO functional groups in the case of the rGO product were reduced when in contact with the reducing agent in suspension and thermally decomposed when heat treated in NH<sub>3</sub> atmosphere.

The different phase of reaction environment could have an effect on the surface energy of the two materials, consequently leading to different morphology.

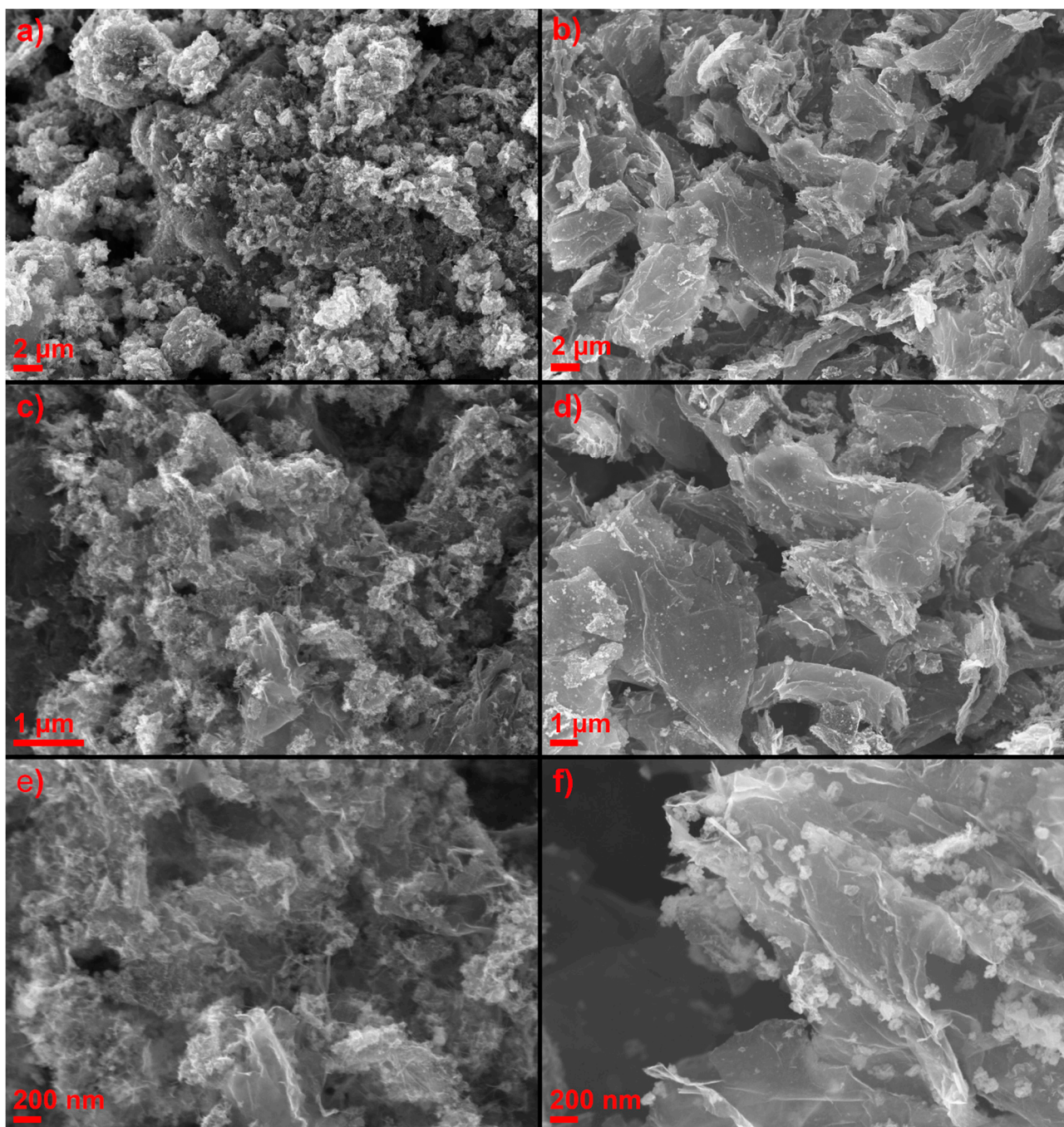


Figure 2. SEM images of Ag-Mn<sub>x</sub>O<sub>y</sub>/rGO (a,c,e) and Ag-Mn<sub>x</sub>O<sub>y</sub>/NGO (b,d,f).

Table 1. BET results of the Ag-Mn<sub>x</sub>O<sub>y</sub>/C catalysts.

Catalysts	BET Surface Area/m <sup>2</sup> g <sup>-1</sup>	External Area/m <sup>2</sup> g <sup>-1</sup>	Micro Pore/m <sup>2</sup> g <sup>-1</sup>	Pore Size/nm
Ag-Mn <sub>x</sub> O <sub>y</sub> /rGO	244.6	236.9	7.6	8.3
Ag-Mn <sub>x</sub> O <sub>y</sub> /NGO	285.7	277.4	8.4	9.8

The SEM images also indicate that the catalyst nanoparticles are better dispersed on rGO than on NGO, where they tend to agglomerate, which could again be due to a

different surface energy. The reason for this phenomenon might be that NGO is more hydrophobic (more reduced, lower oxygen content) than rGO, which hinders non-covalent interactions between substrate and nanoparticle. In addition, Ag-Mn<sub>x</sub>O<sub>y</sub>/rGO shows branch- or stick-like particles on the rGO sheets, attributable to MnO<sub>2</sub>, which were also described in other studies by Tang et al. [14] and Wu et al. [23]. In contrast, the particles on the NGO look more like spheres. It is known that the electrocatalytic activity of manganese oxides in alkaline media highly depends not only on the crystal structure but also on the morphology. Nanowires/nanorods are found to represent the most active form [18,19]. Ag is likely to be present only in very small or amorphous particles, accompanying the XRD results [23].

EDS is used to estimate the elemental composition of Ag-Mn<sub>x</sub>O<sub>y</sub>/rGO and Ag-Mn<sub>x</sub>O<sub>y</sub>/NGO. As can be seen in Table 2, Figures S2 and S3, C, O, Mn, and Ag were detected for both catalyst samples. In addition, a small quantity of nitrogen was traced for the NGO-supported material, which is due to nitrogen doping with ammonia. The higher oxygen content (and therefore lower C content) in the Ag-Mn<sub>x</sub>O<sub>y</sub>/rGO sample than in Ag-Mn<sub>x</sub>O<sub>y</sub>/NGO may be due to more oxygen functional groups in the rGO material [14]. This reinforces the assumption from the XRD that the NGO materials are more reduced. ICP-MS and AAS analyses were also performed to examine the exact quantities of Mn and Ag. The determined values agree relatively well with the theoretically calculated values of 9.8 wt.% for Ag and 13.3 wt.% for Mn. A little more Mn is always detected in the Ag-Mn<sub>x</sub>O<sub>y</sub>/rGO sample, which may be due to residual impurities from the GO synthesis. The lower Ag content obtained by AAS compared to ICP-MS is explained by presuming that a portion of it is bound in the precipitate formed by the splitting.

**Table 2.** Elemental composition results of the Ag-Mn<sub>x</sub>O<sub>y</sub>/C catalysts (wt.%).

Catalysts	ICP-MS		AAS		EDS				
	Mn	Ag	Mn	Ag	Mn	Ag	C	O	N
Ag-Mn <sub>x</sub> O <sub>y</sub> /rGO	13.81	9.51	14.99	7.85	20.31	11.96	30.91	36.82	-
Ag-Mn <sub>x</sub> O <sub>y</sub> /NGO	11.64	9.05	12.63	7.45	12.80	9.52	59.28	17.93	0.47

The reduction process of the graphene derivatives also impacts the chemical composition and consequently thermal stability of the graphene-based materials. In order to test thermal stability and decomposition, evolved gas analysis using TGA coupled with MS was performed in oxidative (O<sub>2</sub>/Ar) and inert atmosphere (Ar). The TGA-MS curves are shown in Figure 3.

The TGA for Ag-Mn<sub>x</sub>O<sub>y</sub>/rGO and Ag-Mn<sub>x</sub>O<sub>y</sub>/NGO in oxidative conditions (Figure 3, left) revealed that both materials have a relatively similar weight loss, which is related to the carbon decomposition. The decomposition occurs at higher temperatures, however, in the case of rGO (between 270 and 550 °C) when compared to NGO (between 270 °C and 420 °C). The remaining mass is therefore directly related to the active material content, which is 33 wt.% and 38 wt.% for Ag-Mn<sub>x</sub>O<sub>y</sub>/rGO and Ag-Mn<sub>x</sub>O<sub>y</sub>/NGO, respectively. The higher value for the NGO-based material can be explained by the larger impurities found by ICP-MS (Table S1). The TGA profiles in inert atmosphere show that both materials reveal the same weight loss at these conditions, but that less material is decomposed than under oxidative conditions (Figure 3, right). The loss above 100 °C is due to a small proportion of evaporation of the water absorbed on the catalysts, as indicated by the *m/z* 18 signal for H<sub>2</sub>O<sup>+</sup> expansion, and due to CO<sub>2</sub> evolution (*m/z* 44). This is attributed to the further graphitization and decomposition of the oxygen functionalities [38]. The Ag-Mn<sub>x</sub>O<sub>y</sub>/NGO sample also shows a small peak for CO loss from 500–800 °C (*m/z* 28). The mass loss can further be assigned to oxygen release caused by Ag-Mn<sub>x</sub>O<sub>y</sub> decomposition. MnO<sub>2</sub> is converted to Mn<sub>2</sub>O<sub>3</sub> and at higher temperatures to MnO [14].

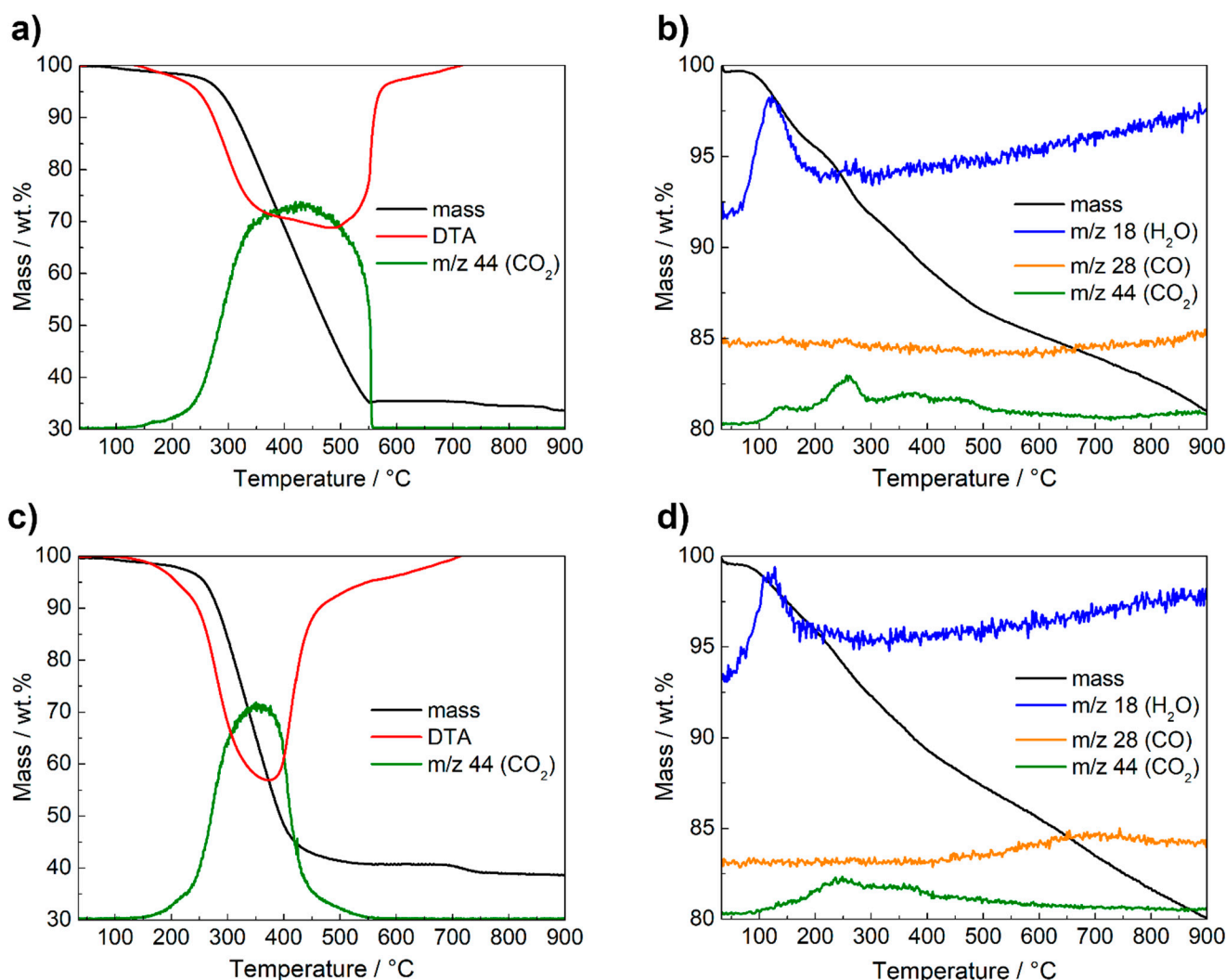


**Figure 3.** TGA-MS curves of Ag-Mn<sub>x</sub>O<sub>y</sub>/rGO (a,b) and Ag-Mn<sub>x</sub>O<sub>y</sub>/NGO (c,d) in O<sub>2</sub>/Ar (left) and Ar atmosphere (right).

## 2.2. Base Cyclic Voltammograms of the Ag-Mn<sub>x</sub>O<sub>y</sub>/C Catalysts

Ex-situ cyclic voltammetry measurements are carried out in de-aerated 1 M KOH electrolyte to investigate the electrochemical properties of Ag-Mn<sub>x</sub>O<sub>y</sub>/rGO and Ag-Mn<sub>x</sub>O<sub>y</sub>/NGO. Base CVs (Figure 4) are recorded at a scan rate of 10 mV s<sup>-1</sup> from 0.1 to 1.0 V vs. RHE after surface cleaning at a faster scan rate (100 mV s<sup>-1</sup>) until stable curves are obtained.

The voltammograms give information about the reduction and oxidation processes of the materials. Both catalysts, Ag-Mn<sub>x</sub>O<sub>y</sub>/rGO and Ag-Mn<sub>x</sub>O<sub>y</sub>/NGO, show a very similar profile. Ag redox peaks are not visible, as these reactions take place only in a higher potential range. Cycling to this potential was not performed, since measurements up to 1.4 V vs. RHE lead to degradation of the catalyst and carbon support [41]. Therefore, the peaks observed in the CVs of the Ag-Mn<sub>x</sub>O<sub>y</sub>/C catalysts are associated with various redox processes of different manganese oxides. The CVs are very similar to that of MnO<sub>2</sub> described in the literature [10,36], confirming the statement from the XRD that the catalyst is present in this form. Cycling from 1.0 V vs. RHE in the cathodic direction, MnO<sub>2</sub> is first reduced to MnOOH, and in lower potential regions, it is reduced to either Mn<sub>2</sub>O<sub>3</sub> or Mn<sub>3</sub>O<sub>4</sub> [10,20,36]. In a further reduction step, the generated Mn(III) species form Mn(OH)<sub>2</sub>. In the anodic scan, the reoxidation reactions proceed. The conversion of Mn(OH)<sub>2</sub> to Mn<sub>2</sub>O<sub>3</sub> (0.4–0.7 V vs. RHE) and MnOOH (0.76 V vs. RHE) takes place first (Equations (1) and (2)). At higher potential ranges from 0.92 V vs. RHE, the conversion of Mn(III) species to MnO<sub>2</sub>

happens (Equations (3) and (4)), which can also overlap with the beginning oxidation of Ag [14,21,23,41,42]. Minor potential shifts can be caused by faster kinetics but also by the interaction of Ag and  $Mn_xO_y$  [10,20].

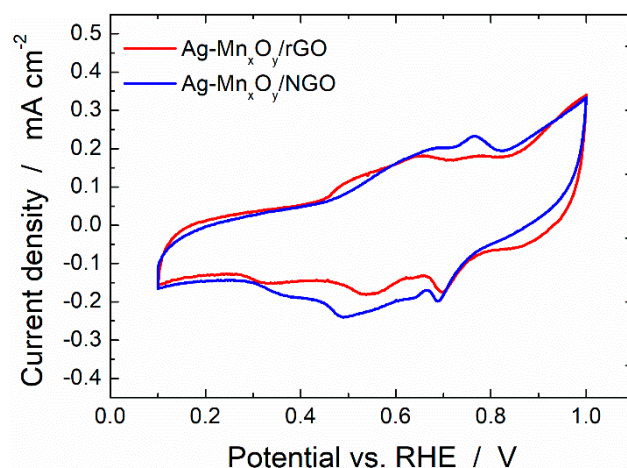
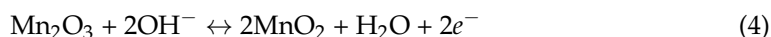
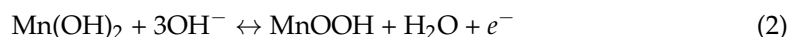
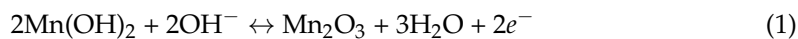


**Figure 4.** Base CV of  $Ag-Mn_xO_y/rGO$  and  $Ag-Mn_xO_y/NGO$  catalysts at  $10 \text{ mV s}^{-1}$  in  $N_2$  purged  $1 \text{ M KOH}$ .

### 2.3. ORR Activity of the Graphene Derivative Supports and $Ag-Mn_xO_y/C$ Catalysts

ORR curves of rGO, NGO,  $Ag-Mn_xO_y/rGO$ , and  $Ag-Mn_xO_y/NGO$  are recorded in  $O_2$  saturated  $1 \text{ M KOH}$  electrolyte at a scan rate of  $10 \text{ mV s}^{-1}$  from  $0.1$ – $1.0 \text{ V}$  vs. RHE to screen the catalyst's activities towards ORR in alkaline media. A commercial Pt/C (30 wt.%) catalyst is analyzed for comparison. Figure 5 shows the potentiodynamic ORR curves of all materials at  $1600 \text{ rpm}$ .

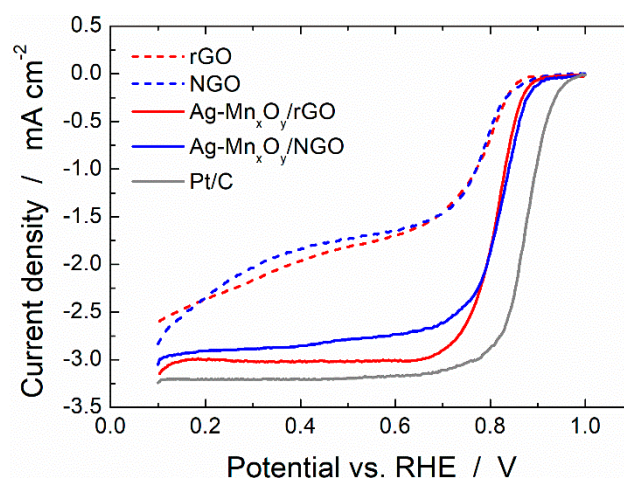


**Figure 5.** Potentiodynamic ORR curves of  $Ag-Mn_xO_y/rGO$  and  $Ag-Mn_xO_y/NGO$  catalysts, support materials, and comm. Pt/C in  $O_2$  saturated  $1 \text{ M KOH}$  at  $10 \text{ mV s}^{-1}$  at  $1600 \text{ rpm}$ .

The onset potential ( $E_{onset}$ ), half-wave potential ( $E_{1/2}$ ), and diffusion limited current density ( $j_D$ ) are significant for the characterization of the ORR activity of a catalyst. The

exact determined values for the different catalysts are listed in Table 3 and a comparison of the ORR performances of various catalysts containing Ag and  $Mn_xO_y$  in literature is given in Table 4.

**Table 3.** Electrochemical characterization results of the graphene derivatives, Ag- $Mn_xO_y$ /C composites, and Pt/C catalyst.

Catalysts	$E_{onset}^{a,b}$ /V vs. RHE	$E_{1/2}^b$ /V vs. RHE	$j_D^{b,c}$ /mA cm <sup>-2</sup>	$n^c$	$k_h^d$ /cm s <sup>-1</sup>
rGO	0.856/0.838	0.772/0.748	-1.96/-1.87	2.51	$0.795 \times 10^{-2}$
NGO	0.871/0.871	0.775/0.787	-1.84/-1.69	2.38	$0.598 \times 10^{-2}$
Ag- $Mn_xO_y$ /rGO	0.889/0.877	0.814/0.791	-3.01/-2.72	3.58	$2.25 \times 10^{-2}$
Ag- $Mn_xO_y$ /NGO	0.904/0.895	0.819/0.796	-2.85/-2.52	3.54	$1.24 \times 10^{-2}$
Pt/C	0.957/-	0.874/-	-3.21/-	3.74	$10.1 \times 10^{-2}$

$E_{onset}$  = onset potential;  $E_{1/2}$  = half-wave potential;  $j_D$  = diffusion limited current density;  $n$  = electron transfer number;  $k_h$  = heterogenous rate constant; <sup>a</sup>  $I = -0.1$  mA cm<sup>-2</sup>; <sup>b</sup> without EtOH/with EtOH; <sup>c</sup>  $E = 0.4$  V vs. RHE; <sup>d</sup>  $E = 0.8$  V vs. RHE.

**Table 4.** Comparison of the ORR performances of various catalysts containing Ag and  $Mn_xO_y$ .

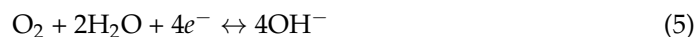
Material	Electrolyte	Onset Potential/ V vs. Reference	Limiting Current Density/mA cm <sup>-2</sup>	Electron Transfer Number/	Tafel Slope/mV dec <sup>-1</sup>	Reference
AgMnOx/C	0.1 M NaOH	-0.045 (vs. Hg/HgO)	-0.92 *	3.69	-	[23]
rGO/MnO <sub>2</sub> /Ag	0.1 M KOH	0.9 (vs. RHE)	3.4	3.90	120.2	[4]
Ag-MnO <sub>x</sub> /G	0.1 M KOH	0.9 (vs. RHE)	-5.51	~4	122 and 57	[16]
Ag-MnO <sub>2</sub> /graphene	0.1 M KOH	0.068 (vs. Hg/HgO)	-5.62	3.90	86	[26]
50%Ag-MnO <sub>2</sub>	0.1 M KOH	0.83 (vs RHE)	-5.50	4.0	89	[21]
Ag-Mn <sub>3</sub> O <sub>4</sub> /C	1 M NaOH	-0.11 (vs. SCE)	approximately 2.6	-	120 and 60	[22]
Ag/Mn <sub>3</sub> O <sub>4</sub> /C	0.1 M NaOH	-	-5.40	3.9-4.0	110 and 55	[14]
Ag-OMS-2	0.1 M KOH	-0.093 (vs. SCE)	-0.784 *	3.94	124.3 and 55.3	[43]
AgMnO <sub>2</sub> /C	1 M KOH	-	approximately -3	2.18	-	[42]
Ag-Mn <sub>x</sub> O <sub>y</sub> /rGO	1 M KOH	0.88 (vs RHE)	-3.01	3.58	118.7 and 54.3	This study
Ag-Mn <sub>x</sub> O <sub>y</sub> /NGO	1 M KOH	0.90 (vs RHE)	-2.85	3.54	129.9 and 58.9	This study

\* Limiting current density is given in mA instead of mA cm<sup>-2</sup>.

The carbon support material itself also has the ability to reduce oxygen, hence they are often investigated as metal-free catalysts [7,8,29]. Comparing the ORR activity of the blank rGO and NGO support material, it can be noticed that they exhibit a very similar  $E_{onset}$ ,  $E_{1/2}$ , and  $j_D$ . It can be further observed that the onset and half-wave potentially shift positively by 30 mV and 40 mV, respectively, and the diffusion limiting current density shifts negatively by 1 mA cm<sup>-2</sup> when decorating both support materials with Ag- $Mn_xO_y$ . The ORR performance of Ag- $Mn_xO_y$ /rGO and Ag- $Mn_xO_y$ /NGO is thereby very close to that for Pt/C and comparable to previously published results of carbon supported Ag- $Mn_xO_y$  catalysts in 1 M KOH [4,22,42]. Furthermore, Ag- $Mn_xO_y$ /rGO shows a slightly more negative limiting current density of -3.01 mA cm<sup>-2</sup> compared to the Ag- $Mn_xO_y$ /NGO (-2.85 mA cm<sup>-2</sup>), whereas the onset (approximately 0.9 V vs. RHE) and half-wave potentials (approximately 0.8 V vs. RHE) are almost the same. This is not only caused by the graphene derivatives, but potentially also by the different structure, morphology, and distribution of the Ag- $Mn_xO_y$  on the support material. With the SEM, it has been shown that Ag- $Mn_xO_y$ /rGO presents a nanorod-like structure and a better distribution of the particles, whereas the particles on Ag- $Mn_xO_y$ /NGO are more clustered and spherical. Nanowires/nanorods are found to represent the most active form [18,19], which could explain the higher activity of the Ag- $Mn_xO_y$ /rGO. In addition, it is known that the active surface of the catalyst where the oxygen can adsorb is of great importance for the performance [10]. The agglomeration of particles on the Ag- $Mn_xO_y$ /NGO results in a loss of surface area, which in turn can decrease the ORR activity. Valim et al. [10] also describe that not only the real active surface but also some intrinsic properties, which are specific for each structure, matter for the electrochemical ORR performance. The kinetics of the oxygen reduction on MnO<sub>2</sub> also depends on the kinetic rate of the reduction to MnOOH, on which O<sub>2</sub> adsorption takes place [26]. Both catalysts show similar reduction processes

in the CVs, which is presumably why the kinetic parameters ( $E_{onset}$ ,  $E_{1/2}$ ) hardly deviate from each other.

Oxygen reduction reaction in alkaline media is a complicated mechanism which can be proceeded either via a direct four-electron pathway (Equation (5)) or the less efficient two-electron hydrogen peroxide pathway (Equation (6)), where  $\text{HO}_2^-$  is reduced in a second step (Equation (7)) [9,10].



Electron transfer numbers ( $n$ ) and the heterogeneous rate constant ( $k_h$ ) are obtained from Koutecky–Levich (K–L) analysis in the diffusion-controlled region of the ORR curves. The voltammograms of all materials at different rotation rates (400 to 2000 rpm) are illustrated in Figure 6 and Figure S4. The current densities in the higher potential region are controlled only by electron-transfer kinetics, not influenced by the rotation rate. At lower potentials, the current densities increase with increasing rotation rate and a plateau is formed, where the current density is limited by mass-transport [44].

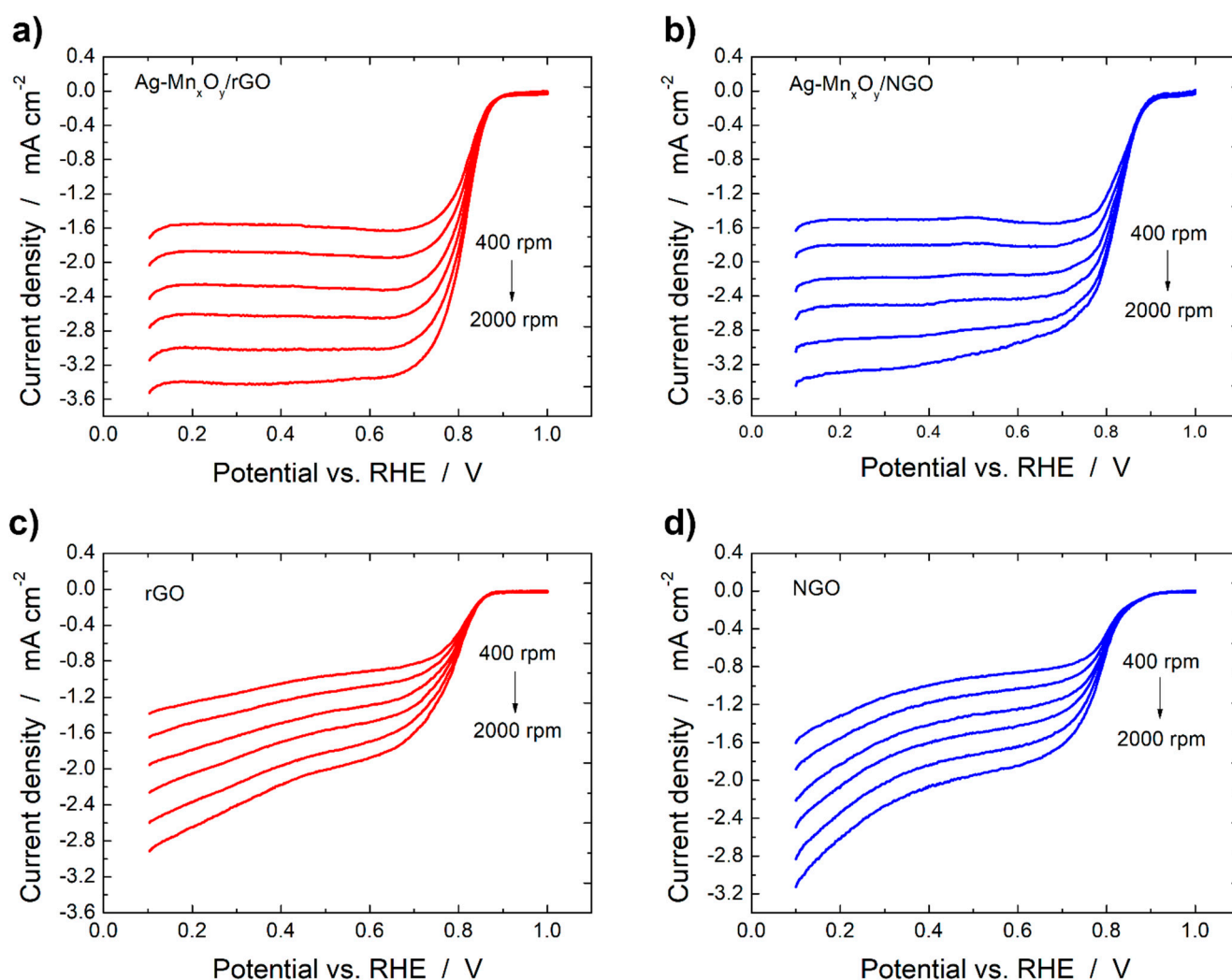


**Figure 6.** Potentiodynamic ORR curves of Ag-Mn<sub>x</sub>O<sub>y</sub>/rGO (a) and Ag-Mn<sub>x</sub>O<sub>y</sub>/NGO (b) catalysts as well as of rGO (c) and NGO (d) support materials in O<sub>2</sub> saturated 1 M KOH at 10 mV s<sup>-1</sup> at different rotation rates.

In Figure 7, the K–L plots of the Ag-Mn<sub>x</sub>O<sub>y</sub>/rGO and Ag-Mn<sub>x</sub>O<sub>y</sub>/NGO catalysts, as well as of the rGO and NGO support materials, obtained by plotting the reciprocal limiting current at 0.4 V vs. RHE (Table S2) against the reciprocal square root of the rotation speed according to K–L Equation (8), are shown. The theoretically calculated lines for a 2-electron or 4-electron reaction are indicated for the purpose of comparison, and the results are summarized in Table 3.

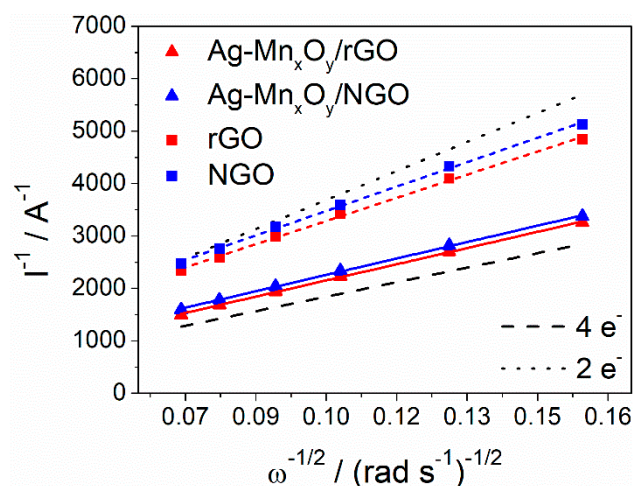


**Figure 7.** Koutecky–Levich plot of Ag-Mn<sub>x</sub>O<sub>y</sub>/rGO, Ag-Mn<sub>x</sub>O<sub>y</sub>/NGO catalysts, and blank support materials.

The ORR of Ag-Mn<sub>x</sub>O<sub>y</sub>/rGO and Ag-Mn<sub>x</sub>O<sub>y</sub>/NGO proceeds via the direct 4-*e*<sup>−</sup> pathway. Ag-Mn<sub>x</sub>O<sub>y</sub>/rGO shows a higher value of 3.58 and Ag-Mn<sub>x</sub>O<sub>y</sub>/NGO also exhibits similar *n* (3.54). The transferred electrons using the commercial Pt/C are only slightly higher (*n* = 3.74). When considering the rate constant (*k<sub>t</sub>*), the Ag-Mn<sub>x</sub>O<sub>y</sub>/C catalysts show faster kinetics than the bare support materials. These results correlate with the findings of the ORR measurements.

Finally, Tafel plots were produced to further investigate the kinetic properties of the Ag-Mn<sub>x</sub>O<sub>y</sub>/C catalysts and Pt/C in comparison with literature (Figure S5). The Tafel slopes were determined at low (region 1) and high overpotentials (region 2). The values are comparable with literature, as pointed out in Table 4, and close to the ones of the commercial Pt/C (107.6 and 53.5 mV dec<sup>−1</sup>).

#### 2.4. Ethanol Tolerance and Catalyst Stability Tests

Although the fuel crossover in ADEFCs is comparatively small, it cannot be completely neglected [45]. Therefore, low interaction between the ORR catalyst and ethanol is targeted. To investigate undesired effects of ethanol crossover, the CV measurements were repeated in a solution mixture of 1 M EtOH and 1 M KOH. Chronoamperometry tests were performed to examine the stability during the ORR. The results are presented in Figure 8 and Figure S6. Compared to Pt/C, which shows a strong peak in the CV with EtOH, the Ag-Mn<sub>x</sub>O<sub>y</sub>/C catalysts are not active for the ethanol oxidation reaction (Figure 8a). Therefore, the ORR of Ag-Mn<sub>x</sub>O<sub>y</sub>/C is affected far less by EtOH (Figure 8b). The catalysts and the support materials display only a slight decrease in diffusion limiting current density and the onset potential hardly changes (Table 3 and Figure S6) when EtOH is present. The influence of EtOH was additionally investigated by instantly adding EtOH after 400 s at an applied potential of 400 mV vs. RHE (Figure 8c). As can be seen, the current of the two Ag-Mn<sub>x</sub>O<sub>y</sub>/C varies only marginally, whereas that of the Pt/C catalyst (inset) drops dramatically at the time of EtOH addition. The remaining current density of Ag-Mn<sub>x</sub>O<sub>y</sub>/NGO after 3600 s is higher compared to Ag-Mn<sub>x</sub>O<sub>y</sub>/rGO, but this is not attributed to the higher tolerance to ethanol, but to the generally higher ORR stability. Nitrogen groups can promote the immobilization and anchoring and thus also the sta-

bility of the metal and metal oxide particles, which might explain the higher stability of Ag-Mn<sub>x</sub>O<sub>y</sub>/NGO [46,47]. As indicated in Figure 8d, Ag-Mn<sub>x</sub>O<sub>y</sub>/rGO presents an overall higher current density loss over time without EtOH compared to Ag-Mn<sub>x</sub>O<sub>y</sub>/NGO, but the decrease in the presence of EtOH is almost the same as without EtOH. Ag-Mn<sub>x</sub>O<sub>y</sub>/NGO, however, shows a much higher current density decrease with EtOH than without.

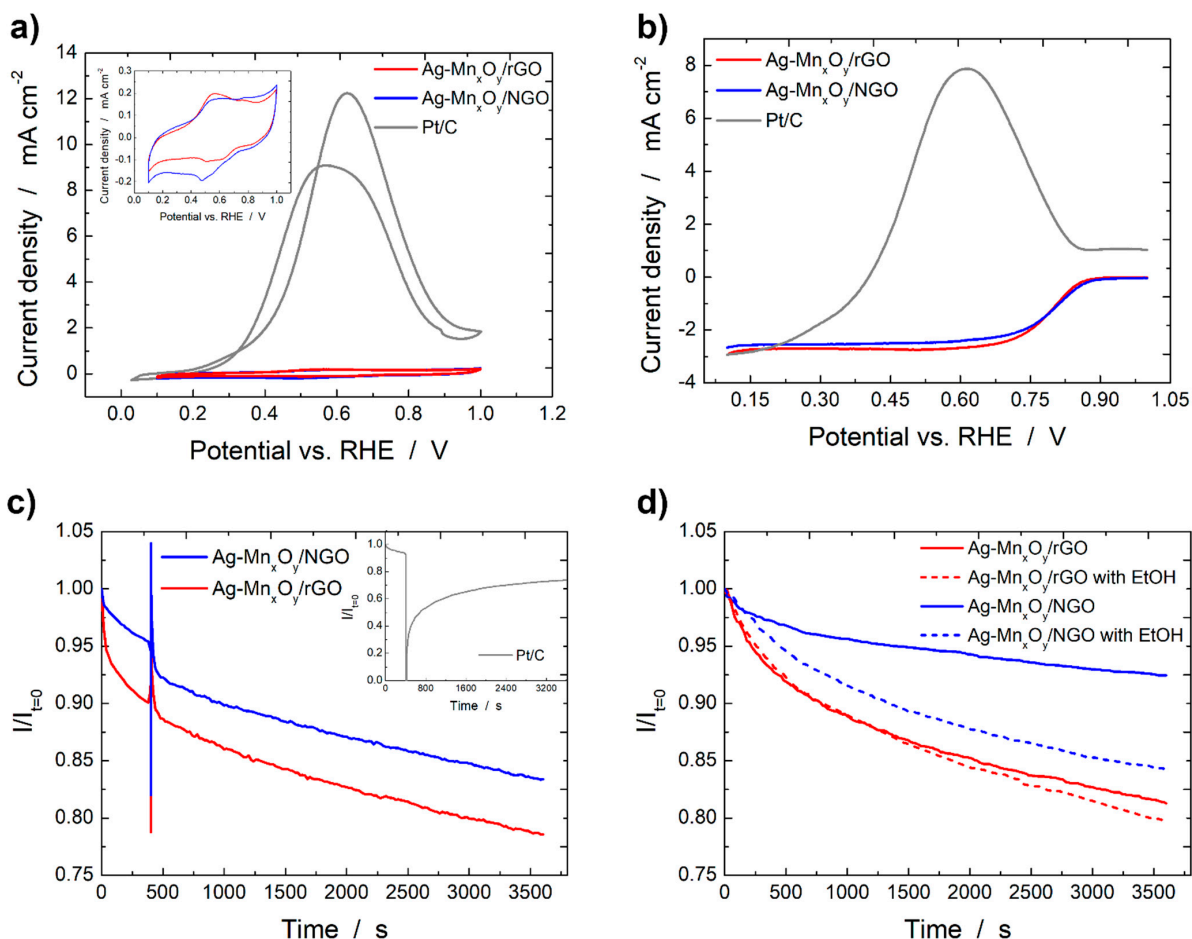


**Figure 8.** CVs (a), ORR curves (b), and influence of EtOH addition during chronoamperometry (c) of Ag-Mn<sub>x</sub>O<sub>y</sub>/rGO, Ag-Mn<sub>x</sub>O<sub>y</sub>/NGO, and Pt/C, as well as stability test (d) of Ag-Mn<sub>x</sub>O<sub>y</sub>/rGO and Ag-Mn<sub>x</sub>O<sub>y</sub>/NGO.

### 3. Materials and Methods

#### 3.1. Materials

Graphene oxide (GO) precursor was prepared via Hummers Method with graphite (Timrex KS44) from Imerys (Bodio, Switzerland). Ethanol (EtOH, 99.9% p.a.) and isopropyl alcohol (2-propanol, ≥99.9%, UV/IR-grade) were supplied by Carl Roth (Karlsruhe, Germany). Nafion<sup>®</sup> Solution (5 wt.% in H<sub>2</sub>O) from Quintech (Göppingen, Germany) was used. Potassium permanganate (KMnO<sub>4</sub>, ≥99.0% p.a.) and silver nitrate (AgNO<sub>3</sub>, ≥99.8% p.a.) were purchased from Merck (Darmstadt, Germany). Potassium hydroxide (KOH, 1.0 M Fixanal 1 L Ampoule) and hydrazine hydrate (N<sub>2</sub>H<sub>4</sub>, reagent grade) were delivered by Sigma Aldrich (Darmstadt, Germany). A commercial Pt/C catalyst (30 wt.% platinum supported on Vulcan) and NH<sub>3</sub> gas (99.8 vol.%) were derived from De Nora North America (NJ, USA) and Messer (Bad Soden, Germany), respectively. An alumina suspension (Al<sub>2</sub>O<sub>3</sub>, 0.05 μm particle size) from MasterPrep<sup>®</sup> Bühler (Lake Bluff, IL, USA) was utilized for polishing the rotating disk electrode. All solutions were prepared with ultrapure water (resistivity ~18 MΩ cm), purified with a Barnstead NANOpureWater Purification System (Dubuque, IA, USA).

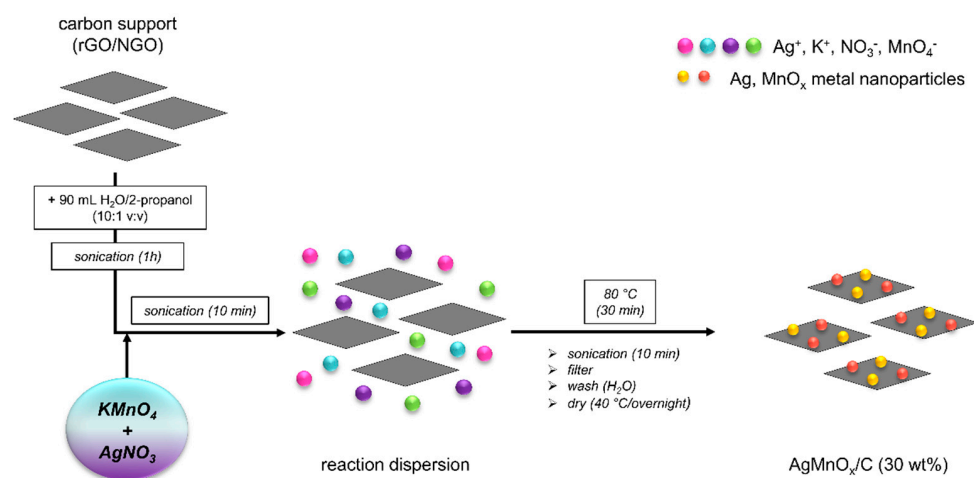
### 3.2. Preparation of Reduced Graphene Oxide (rGO) and N-Doped Graphene Oxide (NGO)

rGO was synthesized according to a slightly modified previously published method [48]. Graphene oxide (17.0 g) was dissolved in Milli-Q water (1.5 L) and put in a 2 L-round bottom flask equipped with a PTFE magnetic stir bar. The round bottom flask was then connected to a reflux condenser and placed on an oil bath. The reaction mixture was slowly heated to 100 °C on a magnetic stirrer equipped with a hot plate (MSH-20D, Witeg, Wertheim, Germany) and stirred at 550 rpm. Then, hydrazine hydrate (170.0 mL) was slowly added through the condenser and the reaction mixture was kept under reflux at 105 °C for 24 h. During the reduction, the reaction mixture changed color from brown to black, which was an indication of chemical reduction. After the reduction, the hot reaction mixture was filtered using an 0.2 µm PTFE membrane filter (Omnipore, Merck, Darmstadt, Germany), the particulate rGO was washed with hot Milli-Q water (1.5 L) and 96 vol.% ethanol (400 mL), and dried at air for 24 h. rGO (4.2 g) was further dried in vacuum overnight at 80 °C.

NGO was synthesized in a split furnace (Carbolite Gero, Neuhusen, Germany) using a previously published method [29]. GO (211 mg) was placed in an alumina crucible and put in a closed quartz tube. The tube was purged with NH<sub>3</sub> at constant flow of 30 mL min<sup>-1</sup> for 10 min at room temperature (RT). The furnace was then subjected to the following heating ramp program in NH<sub>3</sub> atmosphere: from RT to 800 °C at the heating rate 10 K min<sup>-1</sup>, then held at 800 °C for 10 min, and lastly let to cool down back to RT at average cooling rate of 5 K min<sup>-1</sup>. The resulting NGO (75 mg) was collected from the crucible and used for the following experiments without further purification.

### 3.3. Preparation of rGO and NGO Supported Ag-Mn<sub>x</sub>O<sub>y</sub> Catalysts

The graphene derivative supported Ag-Mn<sub>x</sub>O<sub>y</sub> catalysts were prepared according to an adapted, simple synthesis route (Scheme 1) [23]. First, the graphene derivatives (rGO or NGO) were thoroughly dispersed in 90 mL solvent solution [ultrapure water/isopropanol 10:1 V/V]. The addition of isopropanol reduces the surface tension of water and allows a better distribution/dispersion of the carbon [49]. After 30 min of ultrasonication, AgNO<sub>3</sub> and KMnO<sub>4</sub> were added to the homogeneous dispersion to achieve the following mass loadings: 10 wt.% Ag and 20 wt.% MnO<sub>x</sub> (MnO<sub>2</sub> is assumed to be the active material). The dispersion was sonicated for 10 min at room temperature followed by 30 min of stirring at 80 °C under reflux. The precipitate was sonicated for 10 min again, filtered, washed with ultrapure water for several times and dried overnight at 40 °C. The samples are denoted as Ag-Mn<sub>x</sub>O<sub>y</sub>/rGO and Ag-Mn<sub>x</sub>O<sub>y</sub>/NGO. A commercial Pt/C (30 wt.% on Vulcan) catalyst is used as reference material.



**Scheme 1.** Schematic synthesis of rGO/NGO supported Ag-Mn<sub>x</sub>O<sub>y</sub> catalysts.

### 3.4. Physicochemical Characterization

Structure characterization was performed by means of X-ray powder diffraction (XRD) analysis. The measurements were conducted on a XRDynamic 500 diffractometer (Anton Paar, Graz, Austria) in Bragg Brentano geometry in the  $2\theta$  range from  $20^\circ$  to  $90^\circ$  with a step size of  $0.02^\circ$  using a Cu-K $\alpha$  X-ray source ( $\lambda = 1.5418 \text{ \AA}$ ). The raw data were background corrected according to Sonnefeld and Visser. Morphology and EDS chemical characterization of the graphene derivative supported Ag-Mn $_x$ O $_y$  catalysts were performed in the scanning field emission electron microscope (SEM) Zeiss ULTRA plus (Jena, Germany). Samples were adhered to a conductive carbon tape placed on an Al stub. Imaging was performed at 2 kV using a secondary electron detector (SE2 or inlens) at a working distance of 6 mm. EDS chemical characterization was done with the help of an Oxford (Abingdon, UK) X-Max SDD detector (calibrated by Co-Standard) inside the SEM at 20 kV using point analysis. The concentration of Ag and Mn was further analyzed by atomic absorption spectroscopy (AAS) and inductively coupled plasma-mass spectrometry (ICP-MS) using an AAS Varian (Palo Alto, CA, USA) AA 240 (settings:  $\lambda = 247.6 \text{ nm}$ ,  $\Delta\lambda = 0.2 \text{ nm}$ ,  $i\text{HC} = 5 \text{ mA}$ ,  $\Phi\text{C}_2\text{H}_2 = 1.5 \text{ mL min}^{-1}$ ,  $\Phi\text{air} = 3.5 \text{ mL min}^{-1}$ ) and ICP-MS Agilent Technologies (Palo Alto, CA, USA) 7900 equipped with a micro mist nebulizer, quartz spray chamber and quadrupole mass analyzer (Ar gas with high-purity argon (5.0) was used at  $15 \text{ L min}^{-1}$  flow rate), respectively. All other trace metal concentrations were also identified by ICP-MS. For the sample preparation, a mixture of approximately 50 mg of the catalyst powder in 25 mL HNO $_3$  and 2 mL of subsequently added H $_2$ O $_2$  was boiled until half of it was evaporated. Afterwards, the mixture was diluted to 50 mL, filtrated ( $0.45 \text{ }\mu\text{m}$ ) and finally diluted 100 times with ultrapure water. The metal concentrations were then derived by a calibration curve using Merck (Darmstadt, Germany) Multi VI ICP/MS standard and the ICP-MS data were processed and analyzed with MassHunter 4.4 software. Specific surface area (SSA) was determined by N $_2$  gas adsorption at 77 K using BET theory on an ASAP 2020 Micromeritics (Norcross, GA, USA) instrument. Samples ( $\sim 70 \text{ mg}$ ) were placed in a glass tube and degassed under vacuum ( $10 \text{ }\mu\text{mHg}$ ) at  $200^\circ \text{C}$  for 4 h. Nitrogen adsorption/desorption isotherms were obtained in a relative pressure range of 0.01 to 0.99. Thermogravimetric (TG) measurements were performed on a Netzsch (Selb, Germany) 449 F3 Jupiter instrument under a dynamic Ar (5.0) or O $_2$ /Ar (20 vol.%) flow with a flow rate of  $50 \text{ mL min}^{-1}$  in a temperature range from  $30^\circ \text{C}$  to  $900^\circ \text{C}$ . A heating rate of  $10 \text{ K min}^{-1}$  was used. Approximately 15 mg of sample were placed in an alumina (Al $_2$ O $_3$ ) crucible. Simultaneously, mass spectrometry of decomposition gases was performed on an MS 403C Aëolos (Netzsch, Selb, Germany) with a SEM Chenneltron detector and system pressure of  $2 \times 10^{-5} \text{ mbar}$ . Decomposition gasses were transferred to the mass spectrometer through a transfer capillary, quartz ID  $75 \text{ }\mu\text{m}$ , which was heated up to  $220^\circ \text{C}$ . The upper limit of the mass spectrometer detector was 100 AMU.

### 3.5. Electrochemical Characterization

Electrochemical ex-situ characterization of the ORR catalysts was performed by means of cyclic voltammetry using a thin film rotation disk electrode (RDE) from PINE Research Instrumentation (AFE5T0GC, Durham, NC, USA) in a standard three-electrode configuration glass cell (Metrohm, Herisau, Switzerland). A reversible hydrogen electrode (RHE, HydroFlex<sup>®</sup>, Gaskatel, Kassel, Germany) served as reference, a platinized titanium rod (Bank Elektronik—Intelligent Controls GmbH, Pohlheim, Germany) was used as a counter electrode, and the RDE covered with a catalyst layer was utilized as the working electrode. A Reference 600TM Potentiostat/Galvanostat/ZRA and software from GAMRY Instruments (Warminster, PA, USA) operated as control unit.

For the preparation of the working electrode, the catalyst powder was dispersed in a mixture of ultrapure water/ethanol absolute/Nafion 5 wt.% (49:49:2 *v/v/v*), resulting in a homogeneous black dispersion (“ink”) after sonification for 30 min [9]. The RDE was polished using an Al $_2$ O $_3$  suspension and rinsed with water before each coating step. After-

wards, 10  $\mu\text{L}$  of the ink was carefully pipetted on the glassy carbon disk ( $0.19635\text{ cm}^2$ ) and dried by rotation at 700 rpm [50]. A final catalyst loading of  $210\text{ }\mu\text{g cm}^{-2}$  was accomplished.

Measurements were conducted in 1 M KOH electrolyte solution at a constant temperature of  $30\text{ }^\circ\text{C}$ . Firstly, cleaning cycles at a scan rate of  $100\text{ mV s}^{-1}$  in a potential range of 0.1 to 1.0 V vs. RHE were recorded in a de-aerated electrolyte solution (purged with  $\text{N}_2$  for 30 min) under continuous flow of  $\text{N}_2$  until constant cycles were obtained. Subsequently, base CVs were examined with a scan rate of  $10\text{ mV s}^{-1}$ . To analyze the activity towards ORR, CVs were carried out in  $\text{O}_2$  saturated electrolyte solution during constant oxygen bubbling at different rotation rates ( $\omega$ ) of 2000, 1600, 1200, 900, 600, and 400 rpm with a scan rate of  $10\text{ mV s}^{-1}$  in a potential range between 0.1 to 1.0 V vs. RHE. For data evaluation, the anodic sweep of each voltammogram is considered and the ORR voltammograms are corrected by subtracting the base CV to eliminate all currents that are not related to the ORR.

Electron transfer numbers ( $n$ ) and the heterogeneous rate constant ( $k_h$ ) were obtained from Koutecky–Levich analysis. The rotation-speed-dependent current-potential data can be applied to construct a Koutecky–Levich plot according to the following equation [51]:

$$\frac{1}{i_{kl}} = \frac{1}{i_k} + \frac{1}{i_{dl}} = \frac{1}{n F A k_h C_r} + \frac{1}{0.62 n F A D_r^{2/3} \nu^{-1/6} C_r \omega^{1/2}} \quad (8)$$

where  $i_{kl}$  is the measured current (A),  $i_k$  is the kinetic current (A),  $i_{dl}$  is the diffusion limiting current (A),  $F$  is the Faraday constant ( $96485\text{ C mol}^{-1}$ ),  $A$  is the geometric area of the RDE ( $0.196\text{ cm}^2$ ),  $D_r$  is the diffusion coefficient of  $\text{O}_2$  in solution ( $1.8 \times 10^{-5}\text{ cm}^2\text{ s}^{-1}$ ),  $\nu$  is the kinematic viscosity ( $0.01\text{ cm}^2\text{ s}^{-1}$ ) in 1 M KOH,  $C_r$  is the bulk concentration of  $\text{O}_2$  in solution ( $7.8 \times 10^{-7}\text{ mol cm}^{-3}$ ), and  $\omega$  is the rotation rate ( $\text{rad s}^{-1}$ ) [52].

The reciprocal of the measured limited current is plotted against the reciprocal square root of the rotation rate. The electron transfer numbers ( $n$ ) and the heterogeneous rate constant ( $k_h$ ) are derived from the slope and the intercept (Equation (8)), respectively [53,54].

### 3.6. Ethanol Tolerance and Catalyst Stability

To determine the ethanol tolerance of the support materials and ORR catalysts, the CV tests were repeated under the same measuring conditions in a mixture of 1 M KOH and 1 M EtOH solution. The chronoamperometric stability measurements were performed in the diffusion limited current region at 1000 rpm for 3600 s at 0.40 V vs. RHE in  $\text{O}_2$  saturated 1 M KOH and a mixture of 1 M KOH/1 M EtOH. Furthermore, the effect of ethanol during the ORR was evaluated by instantaneously inserting EtOH (2.92 mL to gain 1 M solution) to the  $\text{O}_2$  saturated 1 M KOH after 400 s.

## 4. Conclusions

The Ag- $\text{Mn}_x\text{O}_y/\text{rGO}$  and Ag- $\text{Mn}_x\text{O}_y/\text{NGO}$  catalysts were successfully prepared by depositing the active material onto the graphene derivatives via a simple adapted synthesis method. The physicochemical analyses have shown that the support material has no influence on the Ag- $\text{Mn}_x\text{O}_y$  crystal structure, but that the morphology of the deposited particles is affected. For Ag- $\text{Mn}_x\text{O}_y/\text{rGO}$  and Ag- $\text{Mn}_x\text{O}_y/\text{NGO}$ ,  $\text{MnO}_2$  and very small or amorphous Ag particles were distributed on the carbon, while the  $\text{MnO}_2$  on the rGO is present in nanorod forms and as spheres on the NGO. The elemental analysis revealed that both catalysts exhibit Mn and Ag concentrations very similar to those calculated theoretically, and that C and O, as well as a small N quantity only for Ag- $\text{Mn}_x\text{O}_y/\text{NGO}$ , were detected.

The electrochemical CV measurements of the Ag- $\text{Mn}_x\text{O}_y/\text{C}$  catalysts showed different redox processes related to Mn(II)/Mn(III) and Mn(III)/Mn(IV). It was demonstrated that the deposition of Ag- $\text{Mn}_x\text{O}_y$  on rGO and NGO increased the ORR activity compared to the bare graphene derivatives. The ORR activity and stability of the Ag- $\text{Mn}_x\text{O}_y/\text{C}$  composites were affected by different physicochemical properties induced by the support materials. Ag- $\text{Mn}_x\text{O}_y/\text{rGO}$  achieved a slightly more negative diffusion limited current

density of  $-3.01 \text{ mA cm}^{-2}$  than  $\text{Ag-Mn}_x\text{O}_y/\text{NGO}$  ( $-2.85 \text{ mA cm}^{-2}$ ), but the onset potential was similar at approximately 0.9 V vs. RHE. The ORR proceeded mainly via the direct 4-electron pathway, regardless of the support material.  $\text{Ag-Mn}_x\text{O}_y/\text{NGO}$  showed higher ORR stability, but  $\text{Ag-Mn}_x\text{O}_y/\text{rGO}$  was more tolerant to ethanol poisoning.

**Supplementary Materials:** The following supporting information can be downloaded at: <https://www.mdpi.com/article/10.3390/catal12070780/s1>, Figure S1: Adsorption/desorption isotherms of  $\text{Ag-Mn}_x\text{O}_y/\text{rGO}$  and  $\text{Ag-Mn}_x\text{O}_y/\text{NGO}$ ; Figure S2: EDX results of  $\text{Ag-Mn}_x\text{O}_y/\text{rGO}$ ; Figure S3: EDX results of  $\text{Ag-Mn}_x\text{O}_y/\text{NGO}$ ; Figure S4: Potentiodynamic ORR curves of comm. Pt/C in  $\text{O}_2$  saturated 1 M KOH at  $10 \text{ mV s}^{-1}$  at different rotation rates; Figure S5: Tafel Plot of  $\text{Ag-Mn}_x\text{O}_y/\text{C}$  composites and Pt/C derived from the ORR curves in  $\text{O}_2$  saturated 1 M KOH at  $10 \text{ mV s}^{-1}$  at different rotation rates; Figure S6: Potentiodynamic ORR curves of  $\text{Ag-Mn}_x\text{O}_y/\text{rGO}$  (a) and  $\text{Ag-Mn}_x\text{O}_y/\text{NGO}$  (b) catalysts and blank support materials (c, d) in  $\text{O}_2$  saturated 1 M KOH at  $10 \text{ mV s}^{-1}$  at 1600 rpm with and without EtOH; Table S1: ICP-MS results of the  $\text{Ag-Mn}_x\text{O}_y/\text{C}$  catalysts; Table S2: Limiting current density of the graphene derivatives,  $\text{Ag-Mn}_x\text{O}_y/\text{C}$  composites and Pt/C catalysts without/with EtOH at different rpm.

**Author Contributions:** Conceptualization, S.W.; methodology, S.W., M.R., B.G., D.G., B.B. and V.H.; validation, V.H. and B.G.; formal analysis, S.W., B.G. and B.B.; investigation, S.W., B.G., M.K., M.R. D.G. and B.B.; resources, V.H., B.G. and B.B.; data curation, S.W., B.G. and B.B.; writing—original draft preparation, S.W., M.R., B.G. and M.K.; writing—review and editing, V.H., B.G., S.W., M.R. and B.B.; visualization, S.W.; supervision, V.H. and B.G.; project administration, V.H. and B.G.; funding acquisition, V.H., B.G., S.W. and B.B. All authors have read and agreed to the published version of the manuscript.

**Funding:** This research was funded by the AUSTRIAN SCIENCE FUND (FWF), grant number I 3871-N37) and by the SLOVENIAN RESEARCH AGENCY (ARRS), grant number P1-0175 and N2-0087, in the frame of the project »Graphene Oxide based MEAs for the Direct Ethanol Fuel Cell«.

**Data Availability Statement:** The data that support the findings of this study are available within the article.

**Acknowledgments:** The authors are grateful to Ferdinand Berger for his assistance in the catalyst synthesis and electrochemical characterization. Open Access Funding by the Austrian Science Fund (FWF).

**Conflicts of Interest:** The authors declare no conflict of interest.

## References

1. Huang, C.-Y.; Lin, J.-S.; Pan, W.-H.; Shih, C.-M.; Liu, Y.-L.; Lue, S.J. Alkaline direct ethanol fuel cell performance using alkali-impregnated polyvinyl alcohol/functionalized carbon nano-tube solid electrolytes. *J. Power Sources* **2016**, *303*, 267–277. [[CrossRef](#)]
2. Kamarudin, M.Z.F.; Kamarudin, S.K.; Masdar, M.S.; Daud, W.R.W. Review: Direct ethanol fuel cells. *Int. J. Hydrogen Energy* **2013**, *38*, 9438–9453. [[CrossRef](#)]
3. An, L.; Zhao, T.S. Transport phenomena in alkaline direct ethanol fuel cells for sustainable energy production. *J. Power Sources* **2017**, *341*, 199–211. [[CrossRef](#)]
4. Lee, K.; Ahmed, M.S.; Jeon, S. Electrochemical deposition of silver on manganese dioxide coated reduced graphene oxide for enhanced oxygen reduction reaction. *J. Power Sources* **2015**, *288*, 261–269. [[CrossRef](#)]
5. Ahmed, M.S.; Jeon, S. Highly Active Graphene-Supported  $\text{Ni}_x\text{Pd}_{100-x}$  Binary Alloyed Catalysts for Electro-Oxidation of Ethanol in an Alkaline Media. *ACS Catal.* **2014**, *4*, 1830–1837. [[CrossRef](#)]
6. Qaseem, A.; Chen, F.; Wu, X.; Johnston, R.L. Pt-free silver nanoalloy electrocatalysts for oxygen reduction reaction in alkaline media. *Catal. Sci. Technol.* **2016**, *6*, 3317–3340. [[CrossRef](#)]
7. Liu, Q.; Zhang, H.; Zhong, H.; Zhang, S.; Chen, S. N-doped graphene/carbon composite as non-precious metal electrocatalyst for oxygen reduction reaction. *Electrochim. Acta* **2012**, *81*, 313–320. [[CrossRef](#)]
8. Ramirez-Barria, C.S.; Fernandes, D.M.; Freire, C.; Villaro-Abalos, E.; Guerrero-Ruiz, A.; Rodríguez-Ramos, I. Upgrading the properties of reduced graphene oxide and nitrogen-doped reduced graphene oxide produced by thermal reduction toward efficient ORR electrocatalysts. *Nanomaterials* **2019**, *9*, 1761. [[CrossRef](#)]
9. Grimmer, I.; Zorn, P.; Weinberger, S.; Grimmer, C.; Pichler, B.; Cermenek, B.; Gebetsroither, F.; Schenk, A.; Mautner, F.-A.; Bitschnau, B.; et al. Ethanol tolerant precious metal free cathode catalyst for alkaline direct ethanol fuel cells. *Electrochim. Acta* **2017**, *228*, 325–331. [[CrossRef](#)]

10. Valim, R.B.; Santos, M.C.; Lanza, M.R.V.; Machado, S.A.S.; Lima, F.H.B.; Calegaro, M.L. Oxygen reduction reaction catalyzed by  $\epsilon$ -MnO<sub>2</sub>: Influence of the crystalline structure on the reaction mechanism. *Electrochim. Acta* **2012**, *85*, 423–431. [[CrossRef](#)]
11. Amer, M.S.; Arunachalam, P.; Ghanem, M.A.; Al-Mayouf, A.M.; Shar, M.A. Enriched active surface structure in nanosized tungsten-cobalt oxides electrocatalysts for efficient oxygen redox reactions. *Appl. Surf. Sci.* **2020**, *513*, 145831. [[CrossRef](#)]
12. Amer, M.S.; Ghanem, M.A.; Arunachalam, P.; Al-Mayouf, A.M.; Hadadi, S.M. Bifunctional electrocatalyst of low-symmetry mesoporous titanium dioxide modified with cobalt oxide for oxygen evolution and reduction reactions. *Catalysts* **2019**, *9*, 836. [[CrossRef](#)]
13. Purwaningsih, H.; Suari, N.M.I.P.; Widiyastuti, W.; Setyawan, H. Preparation of rGO/MnO<sub>2</sub> Composites through Simultaneous Graphene Oxide Reduction by Electrophoretic Deposition. *ACS Omega* **2022**, *7*, 6760–6767. [[CrossRef](#)] [[PubMed](#)]
14. Tang, Q.; Jiang, L.; Qi, J.; Jiang, Q.; Wang, S.; Sun, G. One step synthesis of carbon-supported Ag/MnyOx composites for oxygen reduction reaction in alkaline media. *Appl. Catal. B Environ.* **2011**, *104*, 337–345. [[CrossRef](#)]
15. Barsuk, D.; Zadick, A.; Chatenet, M.; Georganakakis, K.; Panagiotopoulos, N.T.; Champion, Y.; Jorge, A.M., Jr. Nanoporous silver for electrocatalysis application in alkaline fuel cells. *Mater. Des.* **2016**, *111*, 528–536. [[CrossRef](#)]
16. Shypunov, I.; Kongi, N.; Kozlova, J.; Matisen, L.; Ritslaid, P.; Sammelselg, V.; Tammeveski, K. Enhanced Oxygen Reduction Reaction Activity with Electrodeposited Ag on Manganese Oxide–Graphene Supported Electrocatalyst. *Electrocatalysis* **2015**, *6*, 465–471. [[CrossRef](#)]
17. Truong, V.M.; Yang, M.-K.; Yang, H. Functionalized Carbon Black Supported Silver (Ag/C) Catalysts in Cathode Electrode for Alkaline Anion Exchange Membrane Fuel Cells. *Int. J. Precis. Eng. Manuf. Green Technol.* **2019**, *6*, 711–721. [[CrossRef](#)]
18. Selvakumar, K.; Kumar, S.M.S.; Thangamuthu, R.; Ganesan, K.; Murugan, P.; Rajput, P.; Jha, S.N.; Bhattacharyya, D. Physicochemical investigation of shape-designed MnO<sub>2</sub> nanostructures and their influence on oxygen reduction reaction activity in alkaline solution. *J. Phys. Chem. C* **2015**, *119*, 6604–6618. [[CrossRef](#)]
19. Sun, W.; Hsu, A.; Chen, R. Carbon-supported tetragonal MnOOH catalysts for oxygen reduction reaction in alkaline media. *J. Power Sources* **2011**, *196*, 627–635. [[CrossRef](#)]
20. Calegaro, M.L.; Lima, F.H.B.; Ticianelli, E.A. Oxygen reduction reaction on nanosized manganese oxide particles dispersed on carbon in alkaline solutions. *J. Power Sources* **2006**, *158*, 735–739. [[CrossRef](#)]
21. Sun, S.; Miao, H.; Xue, Y.; Wang, Q.; Li, S.; Liu, Z. Oxygen reduction reaction catalysts of manganese oxide decorated by silver nanoparticles for aluminum-air batteries. *Electrochim. Acta* **2016**, *214*, 49–55. [[CrossRef](#)]
22. Liu, J.; Liu, J.; Song, W.; Wang, F.; Song, Y. The role of electronic interaction in the use of Ag and Mn<sub>3</sub>O<sub>4</sub> hybrid nanocrystals covalently coupled with carbon as advanced oxygen reduction electrocatalysts. *J. Mater. Chem. A* **2014**, *2*, 17477–17488. [[CrossRef](#)]
23. Wu, Q.; Jiang, L.; Qi, L.; Yuan, L.; Wang, E.; Sun, G. Electrocatalytic activity and stability of Ag-MnOx/C composites toward oxygen reduction reaction in alkaline solution. *Electrochim. Acta* **2014**, *123*, 167–175. [[CrossRef](#)]
24. Sun, Y.; Yang, M.; Pan, J.; Wang, P.; Li, W.; Wan, P. Manganese dioxide-supported silver bismuthate as an efficient electrocatalyst for oxygen reduction reaction in zinc-oxygen batteries. *Electrochim. Acta* **2016**, *197*, 68–76. [[CrossRef](#)]
25. Marukawa, R.; Kiso, T.; Shimizu, T.; Katayama, Y.; Nakayama, M. Layered Manganese Dioxide Thin Films Intercalated with Ag<sup>+</sup> Ions Reduceable In Situ for Oxygen Reduction Reaction. *ACS Omega* **2022**, *7*, 15854–15861. [[CrossRef](#)] [[PubMed](#)]
26. Liu, S.; Qin, X. Preparation of a Ag—MnO<sub>2</sub>/graphene composite for the oxygen reduction reaction in alkaline solution. *RSC Adv.* **2015**, *5*, 15627–15633. [[CrossRef](#)]
27. Marcano, D.C.; Kosynkin, D.V.; Berlin, J.M.; Sinitskii, A.; Sun, Z.; Slesarev, A.; Alemany, L.B.; Lu, W.; Tour, J.M. Improved synthesis of graphene oxide. *ACS Nano* **2010**, *4*, 4806–4814. [[CrossRef](#)]
28. Naderi, H.R.; Sobhani-Nasab, A.; Rahimi-Nasrabadi, M.; Ganjali, M.R. Decoration of nitrogen-doped reduced graphene oxide with cobalt tungstate nanoparticles for use in high-performance supercapacitors. *Appl. Surf. Sci.* **2017**, *423*, 1025–1034. [[CrossRef](#)]
29. Nosan, M.; Löffler, M.; Jerman, I.; Kolar, M.; Katsounaros, I.; Genorio, B. Understanding the Oxygen Reduction Reaction Activity of Quasi-1D and 2D N-Doped Heat-Treated Graphene Oxide Catalysts with Inherent Metal Impurities. *ACS Appl. Energy Mater.* **2021**, *4*, 3593–3603. [[CrossRef](#)]
30. Tasdemir, A.; Kopuklu, B.B.; Kirlioglu, A.C.; Alkan Gursel, S.; Yurum, A. The influence of nitrogen doping on reduced graphene oxide as highly cyclable Li-ion battery anode with enhanced performance. *Int. J. Hydrogen Energy* **2021**, *46*, 11865–11877. [[CrossRef](#)]
31. Lu, Z.-J.; Bao, S.-J.; Gou, Y.-T.; Cai, C.-J.; Ji, C.-C.; Xu, M.-W.; Song, J.; Wang, R. Nitrogen-doped reduced-graphene oxide as an efficient metal-free electrocatalyst for oxygen reduction in fuel cells. *RSC Adv.* **2013**, *3*, 3990–3995. [[CrossRef](#)]
32. Dong, Y.; Deng, Y.; Zeng, J.; Song, H.; Liao, S. A high-performance composite ORR catalyst based on the synergy between binary transition metal nitride and nitrogen-doped reduced graphene oxide. *J. Mater. Chem. A* **2017**, *5*, 5829–5837. [[CrossRef](#)]
33. Liu, Y.; Li, J.; Li, W.; Li, Y.; Chen, Q.; Zhan, F. Nitrogen-doped graphene aerogel-supported spinel CoMn<sub>2</sub>O<sub>4</sub> nanoparticles as an efficient catalyst for oxygen reduction reaction. *J. Power Sources* **2015**, *299*, 492–500. [[CrossRef](#)]
34. Linge, J.M.; Erikson, H.; Sarapuu, A.; Merisalu, M.; Rahn, M.; Matisen, L.; Sammelselg, V.; Tammeveski, K. Electroreduction of oxygen on nitrogen-doped graphene oxide supported silver nanoparticles. *J. Electroanal. Chem.* **2017**, *794*, 197–203. [[CrossRef](#)]
35. Cao, Y.L.; Yang, H.X.; Ai, X.P.; Xiao, L.F. The mechanism of oxygen reduction on MnO<sub>2</sub>-catalyzed air cathode in alkaline solution. *J. Electroanal. Chem.* **2003**, *557*, 127–134. [[CrossRef](#)]

36. Lima, F.H.B.; Calegaro, M.L.; Ticianelli, E.A. Electrocatalytic activity of manganese oxides prepared by thermal decomposition for oxygen reduction. *Electrochim. Acta* **2007**, *52*, 3732–3738. [[CrossRef](#)]
37. Yasin, G.; Arif, M.; Shakeel, M.; Dun, Y.; Zuo, Y.; Khan, W.Q.; Tang, Y.; Khan, A.; Nadeem, M. Exploring the Nickel–Graphene Nanocomposite Coatings for Superior Corrosion Resistance: Manipulating the Effect of Deposition Current Density on its Morphology, Mechanical Properties, and Erosion-Corrosion Performance. *Adv. Eng. Mater.* **2018**, *20*, 1701166. [[CrossRef](#)]
38. Gorgieva, S.; Osmić, A.; Hribernik, S.; Božič, M.; Svetec, J.; Hacker, V.; Wolf, S.; Genorio, B. Efficient chitosan/nitrogen-doped reduced graphene oxide composite membranes for direct alkaline ethanol fuel cells. *Int. J. Mol. Sci.* **2021**, *22*, 1740. [[CrossRef](#)]
39. Tian, K.; Su, Z.; Wang, H.; Tian, X.; Huang, W.; Xiao, C. N-doped reduced graphene oxide/waterborne polyurethane composites prepared by in situ chemical reduction of graphene oxide. *Compos. Part A Appl. Sci. Manuf.* **2017**, *94*, 41–49. [[CrossRef](#)]
40. Li, P.-C.; Hu, C.-C.; Noda, H.; Habazaki, H. Synthesis and characterization of carbon black/manganese oxide air cathodes for zinc-air batteries: Effects of the crystalline structure of manganese oxides. *J. Power Sources* **2015**, *298*, 102–113. [[CrossRef](#)]
41. Grimmer, C.; Zacharias, R.; Grandi, M.; Pichler, B.; Kaltenboeck, I.; Gebetsroither, F.; Wagner, J.; Cermenek, B.; Weinberger, S.; Schenk, A.; et al. A Membrane-Free and Practical Mixed Electrolyte Direct Borohydride Fuel Cell. *J. Electrochem. Soc.* **2016**, *163*, F278–F283. [[CrossRef](#)]
42. Chaiburi, C.; Cermenek, B.; Pichler, B.E.; Grimmer, C.; Hacker, V. Ethanol: Tolerant Oxygen Reduction Reaction Catalysts in Alkaline Media. *J. Electrochem. Energy Convers. Storage* **2019**, *16*, 021004. [[CrossRef](#)]
43. Huang, H.; Meng, Y.; Labonte, A.; Doble, A.; Suib, S.L. Large-scale synthesis of silver manganese oxide nanofibers and their oxygen reduction properties. *J. Phys. Chem. C* **2013**, *117*, 25352–25359. [[CrossRef](#)]
44. Du, C.; Tan, Q.; Yin, G.; Zhang, J. Rotating Disk Electrode Method. In *Rotating Electrode Methods and Oxygen Reduction Electrocatalysts*; Elsevier: Amsterdam, The Netherlands, 2014; pp. 171–198.
45. Zakaria, Z.; Kamarudin, S.K.; Timmiati, S.N. Membranes for direct ethanol fuel cells: An overview. *Appl. Energy* **2016**, *163*, 334–342. [[CrossRef](#)]
46. Erikson, H.; Sarapuu, A.; Tammeveski, K. Oxygen Reduction Reaction on Silver Catalysts in Alkaline Media: A Minireview. *ChemElectroChem* **2019**, *6*, 73–86. [[CrossRef](#)]
47. Jalili, S.; Goliaei, E.M.; Schofield, J. Silver cluster supported on nitrogen-doped graphene as an electrocatalyst with high activity and stability for oxygen reduction reaction. *Int. J. Hydrogen Energy* **2017**, *42*, 14522–14533. [[CrossRef](#)]
48. Stankovich, S.; Dikin, D.A.; Piner, R.D.; Kohlhaas, K.A.; Kleinhammes, A.; Jia, Y.; Wu, Y.; Nguyen, S.B.T.; Ruoff, R.S. Synthesis of graphene-based nanosheets via chemical reduction of exfoliated graphite oxide. *Carbon* **2007**, *45*, 1558–1565. [[CrossRef](#)]
49. Rafati, A.A.; Bagheri, A.; Najafi, M. Experimental data and correlation of surface tensions of the binary and ternary systems of water + acetonitrile + 2-propanol at 298.15 K and atmospheric pressure. *J. Chem. Eng. Data* **2010**, *55*, 4039–4043. [[CrossRef](#)]
50. Garsany, Y.; Singer, I.L.; Swider-Lyons, K.E. Impact of film drying procedures on RDE characterization of Pt/VC electrocatalysts. *J. Electroanal. Chem.* **2011**, *662*, 396–406. [[CrossRef](#)]
51. Cheng, F.; Su, Y.; Liang, J.; Tao, Z.; Chen, J. MnO<sub>2</sub>-based nanostructures as catalysts for electrochemical oxygen reduction in alkaline media. *Chem. Mater.* **2010**, *22*, 898–905. [[CrossRef](#)]
52. Qiao, J.; Xu, L.; Shi, P.; Zhang, L.; Baker, R.; Zhang, J. Effect of KOH concentration on the oxygen reduction kinetics catalyzed by heat-treated co-pyridine/C electrocatalysts. *Int. J. Electrochem. Sci.* **2013**, *8*, 1189–1208.
53. Vincent, I.; Bessarabov, D. Electrochemical characterization and oxygen reduction kinetics of Cu-incorporated cobalt oxide catalyst. *Int. J. Electrochem. Sci.* **2016**, *11*, 8002–8015. [[CrossRef](#)]
54. Masa, J.; Batchelor-McAuley, C.; Schuhmann, W.; Compton, R.G. Koutecky-Levich analysis applied to nanoparticle modified rotating disk electrodes: Electrocatalysis or misinterpretation? *Nano Res.* **2014**, *7*, 71–78. [[CrossRef](#)]